nature climate change

SUPPLEMENTARY INFORMATION

DOI: 10.1038/NCLIMATE2132

Cessation of deep convection in the open Southern Ocean under anthropogenic climate change

Supplementary Information for:

Cessation of deep convection in the open Southern Ocean under anthropogenic climate change

Casimir de Lavergne, Jaime B. Palter, Eric D. Galbraith, Raffaele Bernardello, Irina Marinov

This pdf file includes:

Supplementary text

Supplementary tables S1-S3

Supplementary figures S1-S8

Supplementary references

1. Additional CM2Mc experiments.

The model used for the additional simulations, CM2Mc[21], is a three-degree version of NOAA GFDL's coupled climate model, ESM2M[31], with a simpler land model (LM2) and excluding the iceberg model[32]. Subgrid-scale oceanic convection is parameterized through enhanced vertical diffusivity (see section 2 and Table S3) within the surface boundary layer scheme, which uses the K-profile parameterization[33]. As described in ref. 34, three ensemble members are run for *Climate Change, Wind stress perturbation* and *Precipitation-evaporation* (*P-E) perturbation* experiments. Each member is started from initial conditions taken 20 years apart from a 1000-year pre-industrial simulation segment performed after the end of the spin-up period.

The *Climate Change* experiments use the historical and RCP8.5 forcing data[35] recommended by the Coupled Model Intercomparison Project-CMIP5[24], so that the boundary conditions are identical to those used in 'historical' and 'rcp8.5' CMIP5 experiments. To compute the time-varying perturbation to the wind stress and to the surface freshwater flux used respectively in the *Wind stress perturbation* and *P-E perturbation* experiments, we start by running an additional *Control* simulation, where greenhouse gases are held constant at pre-industrial (1860) levels. We next compute the anomalies in vector wind stress and precipitative-evaporative flux as the differences in monthly means between the *Climate Change* and *Control* simulations. In order to remove the interannual signal caused by the main climate modes of variability, we smooth these anomalies by calculating 20-year running means, for each month, over the period 1860-2100. The smoothed anomalies are then applied at each ocean time step, restricted to the 90°S-40°S region in the case of the *P-E perturbation*. In the *Wind stress perturbation* runs, the wind stress anomalies are applied only when the momentum fluxes are passed from the atmosphere to the

ocean and do not directly interfere with any other process, including buoyancy forcing calculated with bulk formulae, as in ref. 36. In both ensembles, the atmosphere does not feel the perturbation except for any feedbacks resulting from changes in ocean circulation.

Figures S4, S5, and S6 document the response of the Southern Ocean to the full climate, wind stress only and P-E only forcings. In particular, Figure S5 shows the time evolution of the maximum Southern Ocean zonal mean westerly wind stress as well as latitudinal profiles of the zonally averaged zonal wind stress and P-E flux in all ensemble experiments for the 2070-2100 period. The difference between *Climate Change* and *Control* curves gives the wind stress or P-E anomalies applied to the ocean in the *Wind stress perturbation* and *P-E perturbation* runs. The *Wind stress perturbation* experiments exhibit no long-term change in the precipitation-evaporation balance, and neither *Wind stress perturbation* nor *P-E perturbation* simulations show significant changes in the sea level pressure field (Figure S5). On the other hand, in the *Climate Change* simulations, both the P-E and sea level pressure meridional contrasts are significantly altered (Figure S5). We note that these simulated changes under RCP8.5 are qualitatively consistent with an amplification of the global water cycle[17] and a southward shift and intensification of Southern Hemisphere extratropical storm tracks in association with the positive SAM trend[18,37].

In the *Wind stress perturbation* ensemble, though the overall ventilation rate of the deep Southern Ocean shows little change (Figure S6), all three members show a migration of the bulk of the deep convection from the Weddell Sea to the Ross Sea. In two of the three members, the last Weddell Sea convection event ends around 2010, and convection establishes almost permanently in the Ross Sea from 2020 onwards. The third member shows some deep

convection in the Weddell Sea until the end of the simulation, though Ross Sea convection predominates after 2050. The change in the location of deep ventilation arises mainly from a change in ocean circulation: the zonal and meridional wind stress perturbations, which are not zonally homogenous, result in a weakening of the Weddell Gyre's barotropic circulation, but a spin-up of the Ross Gyre. The reduced Ekman upwelling within the Weddell Gyre deepens the pycnocline and increases the stability of the water column there. The opposite is true for the Ross Gyre.

2. Representation of convective and land ice processes in CMIP5 models.

Coarse-resolution, hydrostatic CMIP5 models must employ a convective parameterization in order to remove gravitational instabilities through vertical mixing, mimicking the effect of the convective plumes that would rapidly homogenize the water column in nature. These parameterizations have proven efficient in reproducing the gross properties of convective chimneys[38]. Table S3 lists the numerical schemes used in the CMIP5 models included in this study. The most common approach is to increase the vertical diffusivity to very high values (e.g. $\sim 10\ m^2.s^{-1}$) in regions of gravitational instability, also allowing for some mixing below the depth of neutral stability (i.e. penetrative convection). Alternatively, non-penetrative convective adjustment, such as the scheme of ref. 39, is also frequently used to restore neutral or stable stratification in the water column. Table S3 reveals in particular that the pre-industrial presence or absence of deep convection does not relate to the numerical choices to parameterize open ocean convective processes.

Land ice, dominated by Antarctic and Greenland ice sheets, is only crudely represented in CMIP5 models. Generally, the treatment of these land-based ice sheets will include a prognostic or prescribed albedo and a simple energy and mass balance scheme that, e.g., transports excess snow accumulating over the continent to the coast as frozen runoff, implying a stable long-term mean ice sheet mass and a closed freshwater cycle[32]. In particular, most models do not explicitly account for the effect of freshwater fed into the ocean through ice-shelf basal melting[40] and iceberg calving[32], despite its potential importance for regional freshwater budgets, sea ice cover and deep ocean ventilation[32,40-42]. Some models[31] now incorporate Lagrangian icebergs[32] that can realistically redistribute iceberg melt away from the coast. The unresolved ocean-ice shelf interactions[43] mean, however, that CMIP5 models cannot simulate the observed and projected mass loss of Antarctic ice shelves in response to ocean warming and ocean circulation changes[19,41]. Thus, none of the CMIP5 models analyzed in this study account for changing rates of glacial melt, likely underestimating the rate of freshening of Southern Ocean surface waters under anthropogenic change[43,44].

3. Assessment of model drift in CMIP5 Southern Ocean simulations.

Though reduced when averaged over a large ensemble of models, drift can be significant in individual model simulations, especially in the deep ocean, due to its long equilibration timescale[45]. Therefore, pre-industrial control simulations have been analyzed for drift in Southern Ocean surface and deep water properties. The drift is estimated as the linear trend over the full length of 'piControl' time series[45], and compared to the 2005-2100 RCP8.5 linear trend (Table S2). Multi-model averages of pre-industrial control and RCP8.5 trends, calculated as the

mean over statistically significant (at the 95% level) individual trends, are also given for the convecting and non-convecting model groups.

Table S2 shows that the multi-model mean drift is one to three orders of magnitude smaller than the RCP8.5 trends for all analyzed variables. The drift in convection area averages a gain of 31,000 km^2 per century across the convecting models, compared to a multi-model mean decreasing trend of –384,000 km^2 per century for the 1860-2100 period. Therefore, model drift does not contribute to the slowdown in ensemble mean deep convection documented in Figure 3. Indeed, the small positive ensemble mean drift in both convection area and normalized convection area implies that the decrease in convection strength under RCP8.5 (Figure 3) would only be reinforced if drift were accounted for.

Ensemble mean drift in southern polar ocean 0-100 m salinity and pycnocline strength is so small that the time series presented in Figure 4 are nearly identical whether linear drift is subtracted from the climate change time series or not. Though insignificant for the ensemble mean, drift can be important for the freshening and stratification of individual models. Therefore, a linear drift was subtracted from the warming-driven trends for each model when constructing Figure S7. This figure shows freshening and stratification during 1860-2100 despite the subtracted drift. The correction mostly affects the GISS-E2-H and CNRM-CM5 models, which have the largest drift-to-trend ratios in upper 100 m salinity and are the only two models simulating surface salinification of the southern polar ocean over the 21st century.

Models	Maximum convection area (10^5 km^2)	Mean convection area (10^5 km^2)	Percentage convective years (%)	Mean number of consecutive convective winters	Mean number of consecutive non-convective winters	Maximum number of consecutive non-convective winters	Latest convective year (historical-rcp85)
ACESS1.0	18.97	10.11	100.0	…	0.0	0	2053
ACCESS1.3	22.25	8.86	93.0	…	0.0	17	2068
BCC-CSM1.1*	23.08	1.87	36.2	2.5	4.3	22	*2125
BCC-CSM1.1m	32.26	8.17	66.7	7.2	3.6	45	2095
CMCC-CESM	13.59	2.51	56.3	5.2	4.0	13	2068
CMCC-CM	13.80	3.33	57.6	11.9	8.2	24	2084
CMCC-CMS	14.80	1.46	29.0	3.7	9.1	39	1993
CNRM-CM5*	16.61	1.39	26.6	11.9	31.2	91	*2027
CSIRO-Mk3.6*	2.18	0.05	1.8	2.3	98.2	161	*1862
FGOALS-g2	2.88	0.35	6.4	1.6	21.8	110	1975
FGOALS-s2	51.21	37.76	100.0	…	0.0	0	2095
GFDL-CM3	37.34	10.23	81.6	19.4	4.6	20	2066
GFDL-ESM2G	35.10	14.04	99.4	…	0.0	3	2081
GFDL-ESM2M	21.07	8.83	96.6	…	0.0	6	2084
GISS-E2-H*	40.09	29.44	100.0	…	0.0	0	*2295
GISS-E2-R*	59.03	47.55	100.0	…	0.0	0	*2300
HadGEM2-CC	7.00	0.85	30.4	2.8	6.4	17	2023
HadGEM2-ES*	4.13	0.49	19.8	2.0	8.1	49	*2015
IPSL-CM5A-LR*	10.00	0.40	11.0	2.8	22.3	231	*2097
IPSL-CM5A-MR	27.01	4.41	67.3	16.8	8.2	21	2062
IPSL-CM5B-LR	4.08	0.19	3.7	2.2	13.5	33	2011
MIROC5	17.55	8.42	99.4	…	0.0	2	2100
MPI-ESM-LR*	13.59	5.46	99.1	…	0.0	2	*2051
MPI-ESM-MR	19.52	8.02	100.0	…	0.0	0	2069
MRI-CGCM3	28.48	17.89	100.0	…	0.0	0	2100
CM2Mc	27.96	7.57	65.7	17.3	7.1	27	1981
BNU-ESM	0.28	0.00	0.0	…	…	…	…
CanESM2	0.24	0.03	0.0	…	…	…	…
CCSM4*	0.24	0.00	0.0	…	…	…	…
CESM1-BGC	0.35	0.00	0.0	…	…	…	…
CESM1-CAM5	0.00	0.00	0.0	…	…	…	…
CESM1-WACCM	0.09	0.00	0.0	…	...	…	…
INMCM4	0.00	0.00	0.0	…	…	…	…
MIROC-ESM	8.19	0.40	15.9	9.0	69.8	531	…
MIROC-ESM-CHEM	0.00	0.00	0.0	…	…	…	…
NorESM1-M	0.03	0.00	0.0	…	…	…	...
NorESM1-ME	0.00	0.00	0.0	…	…	…	…

Table S1: **Characteristics of convection in CMIP5 models and CM2Mc.**

All metrics were calculated from the full extent of pre-industrial model outputs, except for the latest convective year (last column), which pertains to climate change simulations, extending from 1860 to 2100 or from 1860 to 2300 in nine models (asterisks). The upper 25 models are

those referred to as ‘convecting’ models while the bottom 11 models are ‘non-convecting’ models. Characteristics of convection in CM2Mc are also given for comparison. Despite the significant convection displayed by MIROC-ESM at the end of its control simulation, this model was classified as non-convecting because no single convective year was found in historical and RCP8.5 experiments (see Table S2). Convective years correspond to a convection area in excess of 100,000 km^2. Two models (GISS-E2-H and GISS-E2-R) show robust convection until 2300, while seven models cease convecting before 2030.

Models	0-100 m salinity (PSS-78.cent^{-1})		Pycnocline strength (g.m^{-3}.cent^{-1})		surface density (g.m^{-3}.cent^{-1})		2000 m density (g.m^{-3}.cent^{-1})		Convection area (10^{5} km^{2}.cent^{-1})	
	piControl	rcp8.5	piControl	rcp8.5	piControl	rcp8.5	piControl	rcp8.5	piControl	hist-rcp8.5
ACCESS1.0	-0.001	**-0.158**	**1.0**	**110.9**	**-8.1**	**-346.3**	**-6.2**	**-33.1**	**0.25**	**-4.68**
ACCESS1.3	**0.007**	**-0.226**	-0.2	**117.8**	**2.1**	**-316.1**	**8.5**	**-43.9**	**-0.82**	**-3.95**
BCC-CSM1.1	**-0.008**	**-0.041**	**0.8**	**35.1**	**-5.5**	**-243.4**	**-4.7**	**-23.9**	-0.02	**-0.99**
BCC-CSM1.1m	**-0.002**	**-0.133**	**1.3**	**45.2**	**-3.2**	**-189.0**	**-4.7**	**-34.1**	0.40	**-5.99**
CMCC-CESM	**-0.005**	**-0.138**	**2.9**	**79.6**	**-6.8**	**-303.1**	**-1.5**	**-15.7**	-0.23	**-1.25**
CMCC-CM	**0.018**	**-0.096**	**-4.2**	**73.4**	**-7.8**	**-307.4**	**-4.2**	**-23.2**	**0.86**	**-2.82**
CMCC-CMS	0.000	**-0.066**	-0.7	**55.9**	0.0	**-274.4**	**-1.3**	**-16.9**	**0.17**	**-1.13**
CNRM-CM5	**-0.022**	**0.013**	**1.7**	**52.5**	**-22.4**	**-298.8**	**-11.1**	**-15.5**	0.00	**-0.86**
CSIRO-MK3.6	-0.001	**-0.267**	**1.9**	**131.3**	**-2.0**	**-354.6**	**7.6**	**-4.3**	**-0.02**	**-0.05**
FGOALS-g2	**0.027**	**-0.164**	0.1	**18.9**	**16.3**	**-284.7**	**27.5**	**-32.5**	0.01	**-0.26**
FGOALS-s2	**0.012**	**-0.456**	**0.8**	**171.1**	**15.9**	**-527.8**	**17.5**	**-53.7**	**0.35**	**-19.71**
GFDL-CM3	**0.004**	**-0.211**	0.0	**134.3**	**-12.4**	**-338.3**	**-9.5**	**-49.9**	**1.61**	**-4.53**
GFDL-ESM2G	-0.003	**-0.395**	0.8	**138.0**	-0.2	**-318.1**	**1.2**	**-18.9**	-0.03	**-6.24**
GFDL-ESM2M	**-0.002**	**-0.116**	0.0	**64.4**	**-3.2**	**-196.5**	**-2.8**	**-21.6**	0.03	**-5.02**
GISS-E2-H	**0.042**	**0.101**	**-7.0**	**-115.0**	**26.8**	**-158.1**	**12.4**	**-22.0**	**0.73**	**-2.62**
GISS-E2-R	0.001	**-0.123**	-0.1	**65.0**	-0.1	**-211.3**	**3.0**	**-50.2**	-0.50	**-13.69**
HADGEM2-CC	-0.001	**-0.293**	-0.3	**134.3**	**7.0**	**-398.2**	**-3.0**	**-45.2**	-0.02	**-0.35**
HADGEM2-ES	**-0.006**	**-0.244**	0.4	**128.7**	**-7.4**	**-424.1**	**-6.1**	**-41.9**	-0.03	**-0.44**
IPSL-CM5A-LR	**0.001**	**-0.066**	**-0.6**	**32.3**	0.2	**-235.6**	**-0.5**	**-19.0**	**0.07**	0.21
IPSL-CM5A-MR	-0.002	**-0.079**	0.2	**30.7**	**-5.6**	**-203.9**	**3.4**	**-16.1**	0.30	**-1.12**
IPSL-CM5B-LR	**0.014**	**-0.096**	**-18.3**	**93.6**	**10.6**	**-343.2**	**-10.0**	**-30.8**	**0.15**	**-0.10**
MIROC5	**0.003**	**-0.164**	**2.7**	**66.4**	**-7.0**	**-187.1**	**-8.7**	**-43.6**	**0.30**	**-2.88**
MPI-ESM-LR	0.000	**-0.111**	**-0.2**	**58.6**	0.3	**-204.8**	**-0.2**	**-28.1**	0.01	**-2.87**
MPI-ESM-MR	0.000	**-0.115**	0.0	**78.4**	**-0.6**	**-171.5**	**-0.8**	**-27.4**	**-0.08**	**-3.85**
MRI-CGCM3	**0.004**	**-0.086**	**-1.1**	**35.4**	**5.1**	**-365.3**	**-4.2**	**-29.9**	**0.46**	**-6.74**
Multimodel mean	0.005	-0.156	-1.3	73.5	-0.4	-288.1	0.1	-29.6	0.31	-3.84
CM2Mc	-0.001	**-0.137**	-1.9	**99.1**	2.8	**-242.2**	**-0.88**	**-20.9**	-0.06	**-3.42**
BNU-ESM	-0.011	**-0.085**	-7.9	**58.6**	-1.1	**-352.7**	**-18.2**	**-40.5**	…	…
CanESM2	**-0.003**	**-0.338**	**1.9**	**180.7**	**-4.8**	**-365.8**	**8.3**	**-4.9**	…	…
CCSM4	**0.007**	**-0.531**	**-1.8**	**303.6**	**2.3**	**-448.0**	**5.1**	**-24.6**	…	…
CESM1-BGC	**0.006**	**-0.411**	0.1	**276.3**	**-1.1**	**-436.4**	**8.1**	**-20.1**	…	…
CESM1-CAM5	**-0.015**	**-0.298**	**4.1**	**231.0**	**-10.9**	**-447.1**	**-4.2**	**-22.4**	…	…
CESM1-WACCM	**0.013**	**-0.387**	**12.7**	**282.8**	**-8.3**	**-467.2**	**9.6**	**-10.0**	…	…
INM-CM4	**0.003**	**-0.076**	**-4.9**	**56.2**	**-1.5**	**-216.2**	**12.4**	**2.6**	…	…
MIROC-ESM	0.002	**-0.227**	**1.7**	**157.1**	**-14.6**	**-283.1**	**-30.6**	**-48.5**	**0.32**	…
MIROC-ESM-CHEM	**-0.029**	**-0.198**	**8.7**	**154.2**	**-19.3**	**-305.1**	**-34.5**	**-51.9**	…	…
NORESM1-M	**0.005**	**-0.382**	-0.2	**75.2**	**-5.6**	**-358.0**	**-2.5**	**-31.1**	…	…
NORESM1-ME	0.008	**-0.439**	**-3.6**	**85.9**	**3.6**	**-351.3**	**-4.8**	**-25.9**	…	…
Multimodel mean	-0.002	-0.307	2.4	169.3	-6.0	-366.4	-4.7	-25.2	…	…

Table S2: Pre-industrial control and RCP8.5 Southern Ocean linear trends in CMIP5 models and CM2Mc.

Upper 100 m salinity and pycnocline strength refer to southern polar ocean annual means, as presented in Figure 4; surface and 2000 m density refer to 90°S-50°S annual mean locally-

referenced potential densities; convection area is as defined in Methods and as presented in Figure 3. Full-length pre-industrial control and 2005-2100 (1860-2100 for the convection area) RCP8.5 linear trends are compared. Statistically significant trends at the 95% level are indicated in bold. Multi-model averages, calculated as the mean over 95%-level significant trends, are also given for the convecting and non-convecting model groups. Note that differing lengths of 'piControl' time series preclude a direct assessment of the drift (and its significance) in ensemble mean properties. The multi-model mean drift is one to three orders of magnitudes smaller than RCP8.5 trends. All convecting models show a significant decrease in convection area over 1860-2100 except IPSL-CM5A-LR, which shows non-significant change over this period but ceases to convect following 2097 (Table S1). The MIROC-ESM models exhibit the strongest drift in 2000 m density: warming and freshening of Southern Ocean deep waters gradually weaken the vertical stability, eventually causing the abrupt convective onset at year 530 of the MIROC-ESM pre-industrial simulation (only 255 years are available for MIROC-ESM-CHEM).

Models	Ocean code	Mixed layer scheme	Treatment of convection
ACESS1.0	MOM4.1	K-profile parameterization (33)	enhanced vertical diffusion
ACCESS1.3	MOM4.1	K-profile parameterization (33)	enhanced vertical diffusion
BCC-CSM1.1	MOM4-L40	K-profile parameterization (33)	enhanced vertical diffusion
BCC-CSM1.1m	MOM4-L40	K-profile parameterization (33)	enhanced vertical diffusion
CMCC-CESM	NEMO(OPA8.2)	Turbulent kinetic energy closure (46,47)	enhanced vertical diffusion
CMCC-CM	NEMO(OPA8.2)	Turbulent kinetic energy closure (46,47)	enhanced vertical diffusion
CMCC-CMS	NEMO(OPA8.2)	Turbulent kinetic energy closure (46,47)	enhanced vertical diffusion
CNRM-CM5	NEMO3.2	Turbulent kinetic energy closure (46,47)	enhanced vertical diffusion
CSIRO-Mk3.6	MOM2.2	Kraus-Turner scheme (48)	convective adjustment (39)
FGOALS-g2	LICOM2	Turbulent kinetic energy closure (49,50)	convective adjustment (39)
FGOALS-s2	LICOM2	Turbulent kinetic energy closure (49,50)	convective adjustment (39)
GFDL-CM3	MOM4.1	K-profile parameterization (33)	enhanced vertical diffusion
GFDL-ESM2G	GOLD	Bulk mixed layer/Turbulent kinetic energy closure (48,51,52)	included in the turbulence closure
GFDL-ESM2M	MOM4.1	K-profile parameterization (33)	enhanced vertical diffusion
GISS-E2-H	HYCOM	K-profile parameterization (33)	enhanced vertical diffusion
GISS-E2-R	Russell	K-profile parameterization (33)	enhanced vertical diffusion
HadGEM2-CC	HadGOM2	Kraus-Turner/K-theory scheme (48,33)	convective adjustment (39)
HadGEM2-ES	HadGOM2	Kraus-Turner/K-theory scheme (48,33)	convective adjustment (39)
IPSL-CM5A-LR	NEMO3.2	Turbulent kinetic energy closure (46,47)	enhanced vertical diffusion
IPSL-CM5A-MR	NEMO3.2	Turbulent kinetic energy closure (46,47)	enhanced vertical diffusion
IPSL-CM5B-LR	NEMO3.2	Turbulent kinetic energy closure (46,47)	enhanced vertical diffusion
MIROC5	COCO4.5	Turbulent kinetic energy closure (53,54,55)	convective adjustment (39)
MPI-ESM-LR	MPI-OM	Richardson number dependent (56)	enhanced vertical diffusion
MPI-ESM-MR	MPI-OM	Richardson number dependent (56)	enhanced vertical diffusion
MRI-CGCM3	MRI.COM3	Turbulent kinetic energy closure (53,54,55)	convective adjustment (39)
CM2Mc	MOM4.1	K-profile parameterization (33)	enhanced vertical diffusion
BNU-ESM	MOM4.1	K-profile parameterization (33)	enhanced vertical diffusion
CanESM2	NCOM	K-profile parameterization (33)	enhanced vertical diffusion
CCSM4	POP2	K-profile parameterization (33)	enhanced vertical diffusion
CESM1-BGC	POP2	K-profile parameterization (33)	enhanced vertical diffusion
CESM1-CAM5	POP2	K-profile parameterization (33)	enhanced vertical diffusion
CESM1-WACCM	POP2	K-profile parameterization (33)	enhanced vertical diffusion
INMCM4	INMOM4	Richardson number dependent (56)	enhanced vertical diffusion
MIROC-ESM	COCO3.4	Turbulent kinetic energy closure (53,54,55)	convective adjustment (39)
MIROC-ESM-CHEM	COCO3.4	Turbulent kinetic energy closure (53,54,55)	convective adjustment (39)
NorESM1-M	MICOM/Bergen	Bulk mixed layer/Turbulent kinetic energy closure (57)	convective adjustment (39)
NorESM1-ME	MICOM/Bergen	Bulk mixed layer/Turbulent kinetic energy closure (57)	convective adjustment (39)

Table S3: Parameterizations of convection in CMIP5 models and CM2Mc.

The numerical treatment of mixed layer physics and convective instabilities is given for each model along with relevant references (numbers). The algorithm of ref. 39 is indicated as the reference for non-penetrative convective adjustment schemes though some models may use slightly different implementations. Information was collected from the ES-DOC model metadata

database available at http://earthsystemcog.org/projects/es-doc-models/comparator_demo, complemented by published model documentation.

Figure S1: Spatial pattern of Southern Ocean deep convection in 25 convecting CMIP5 models. For each model, the September mixed layer depth (shading) and 25% and 75% September sea ice concentration contours (light grey lines) are shown as averages over pre-industrial control years during which the convection area exceeds half of its overall maximum.

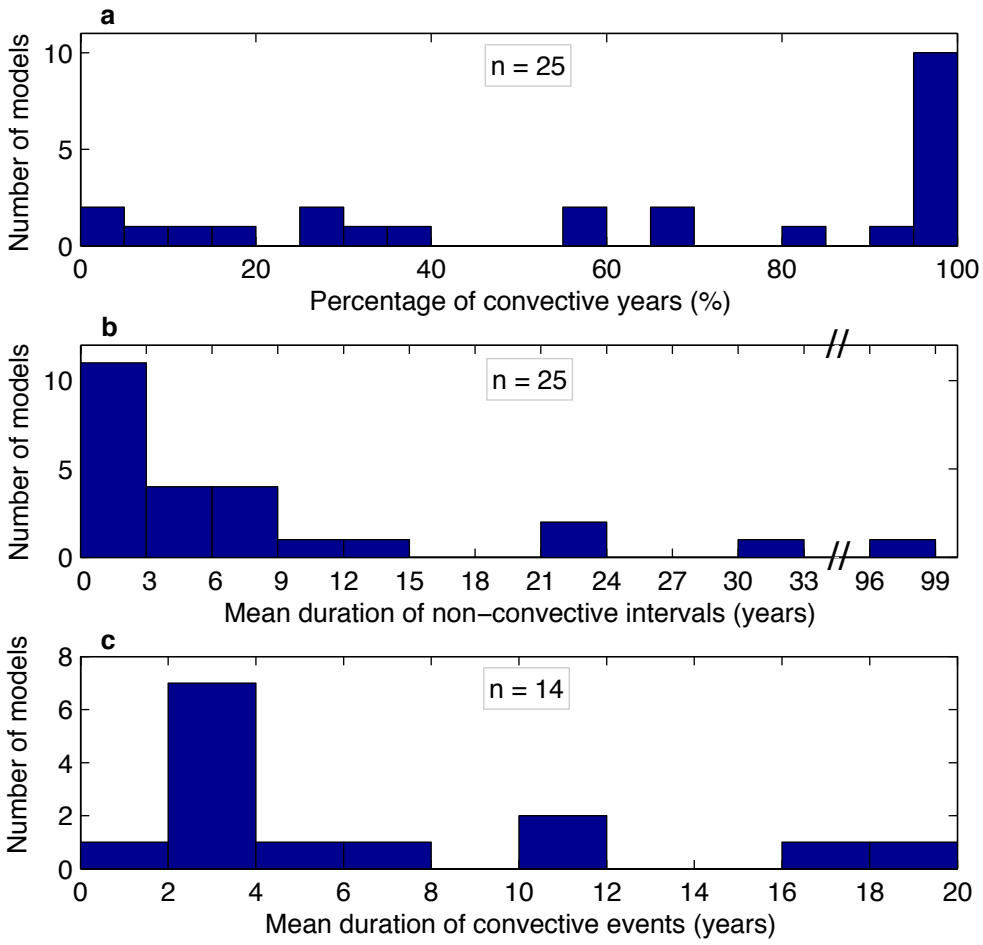

Figure S2: Frequency and duration of simulated Southern Ocean convective events under pre-industrial conditions. Distribution of the 25 convecting CMIP5 models according to (**a**) percentage of convective years and (**b**) mean duration of non-convective intervals, and (**c**) distribution of 14 intermittently convecting CMIP5 models according to duration of convection events. Note that both the frequency and the duration of convective events are highly variable across models. Eleven models simulate convection almost every winter. The 14 models that allow only intermittent convection show a mean duration of convective periods ranging between one and 19 consecutive winters, and a mean hiatus between events of three to 98 years.

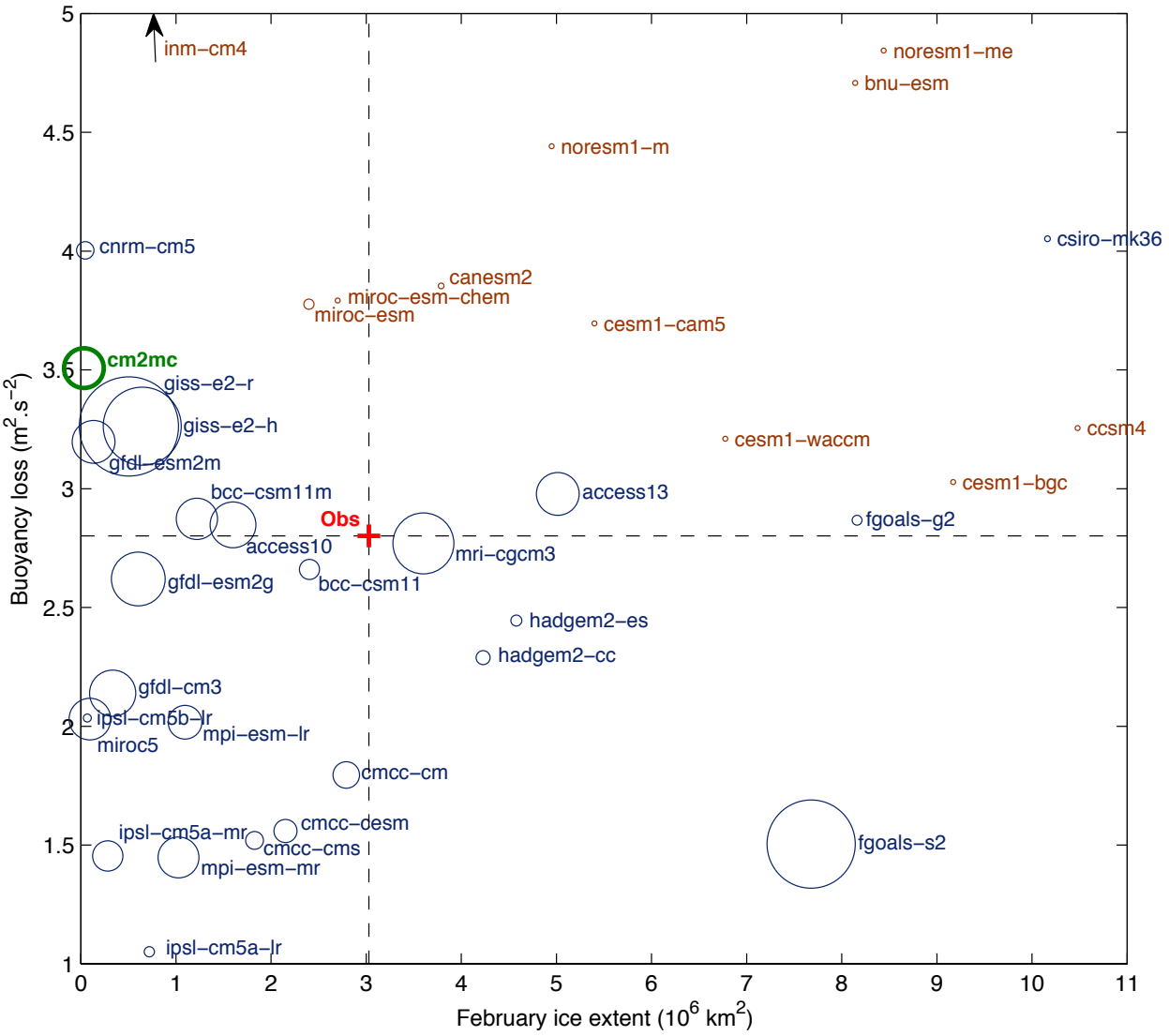

Figure S3: Southern Ocean stratification versus February ice extent in the CMIP5 model suite for the 1976-2005 period. Pre-industrial mean convection area reflected by the size of the circle for each model. The stratification is measured by the buoyancy loss necessary for convection to reach a depth of 3000 m in September, calculated as $\frac{g}{\rho_0}\int_0^{3000}\left[\sigma_\theta(3000m)-\sigma_\vartheta(z)\right]dz$, averaged over 55°S-90°S; σ_θ is the potential density referenced to the surface, and g, ρ_0 are constants. Sea ice extent refers to the area over which the sea ice concentration is larger than 15 %. All model variables are averaged over 1976-2005. A corresponding observational estimate (red cross) is

indicated, where the stratification is calculated from the CARS[28] September climatology and the observed February sea ice extent is the 1979-2005 average (data from the National Snow and Ice Data Center[58]). The 11 models with no significant convective activity (brown) tend to have either strong vertical stratification or large summer sea ice coverage or a combination of both relative to observations. The CM2Mc model (three-member ensemble mean) is shown in green.

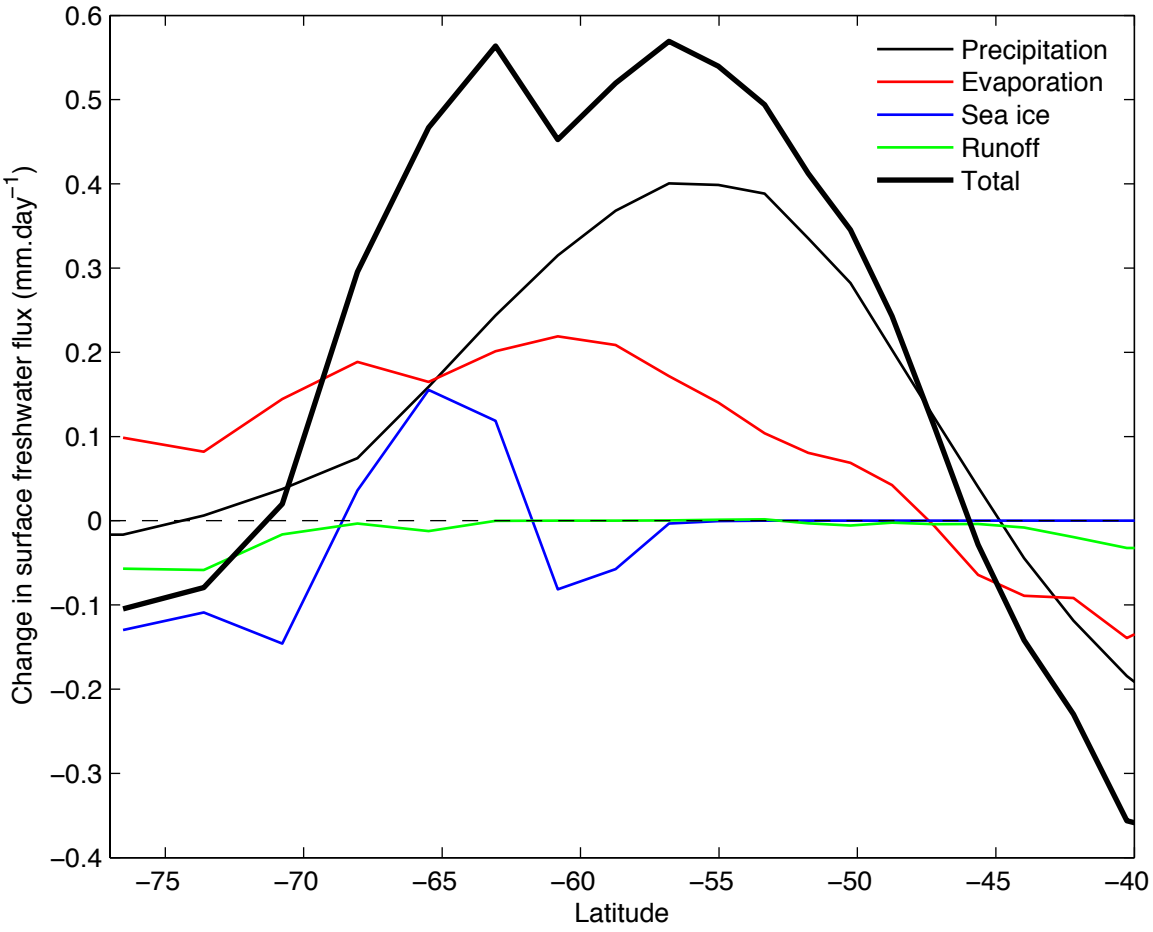

Figure S4: Changes in surface freshwater fluxes (mm.day^{-1}) in the CM2Mc *Climate Change* model simulations. Zonal mean total change (thick black line) and contributions due to precipitation (black), evaporation (red), sea ice melt (blue; negative values mean less melt or more ice growth) and runoff (green). Positive values correspond to an increase in freshwater input to the surface ocean. Ensemble multi-annual mean of three simulations presented for years 2070-2100 minus 1860-1890 (the same quantity calculated in the *Control* simulations showed the model drift to be negligible). Precipitative-evaporative freshening changes dominate between 68°S and 46°S.

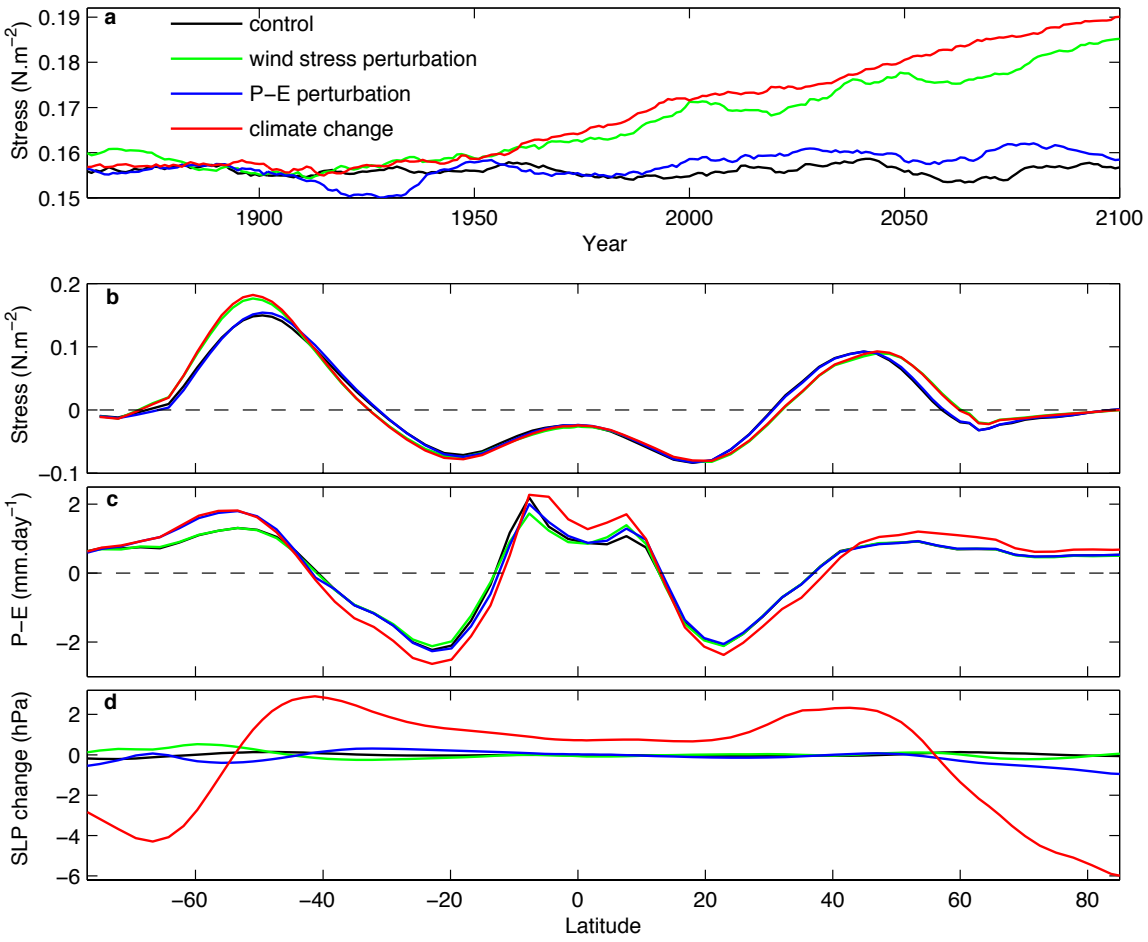

Figure S5: Changes in low-level atmospheric circulation and hydrological cycle in the CM2Mc ensemble experiments. **a**, Time evolution of the 20-year running mean maximum Southern Ocean zonal mean zonal wind stress. Zonal mean (**b**) zonal wind stress and (**c**) precipitation minus evaporation (P-E) averaged over 2070-2100. **d**, Difference in zonal mean sea level pressure (SLP) between years 2070-2100 and 1860-1890. All are averaged over (black) *Control*, (green) *Wind stress perturbation*, (blue) *P-E perturbation* and (red) *Climate Change* three-member ensembles. Under RCP8.5 (red curves), the P-E meridional gradients deepen and the high latitude maxima in P-E shift poleward (c). The deepening of the meridional gradient in SLP at about 53°S (d) signals the positive long-term change in the SAM index, which is accompanied by a strengthening and southward shift of the low-level atmospheric circulation (a,b).

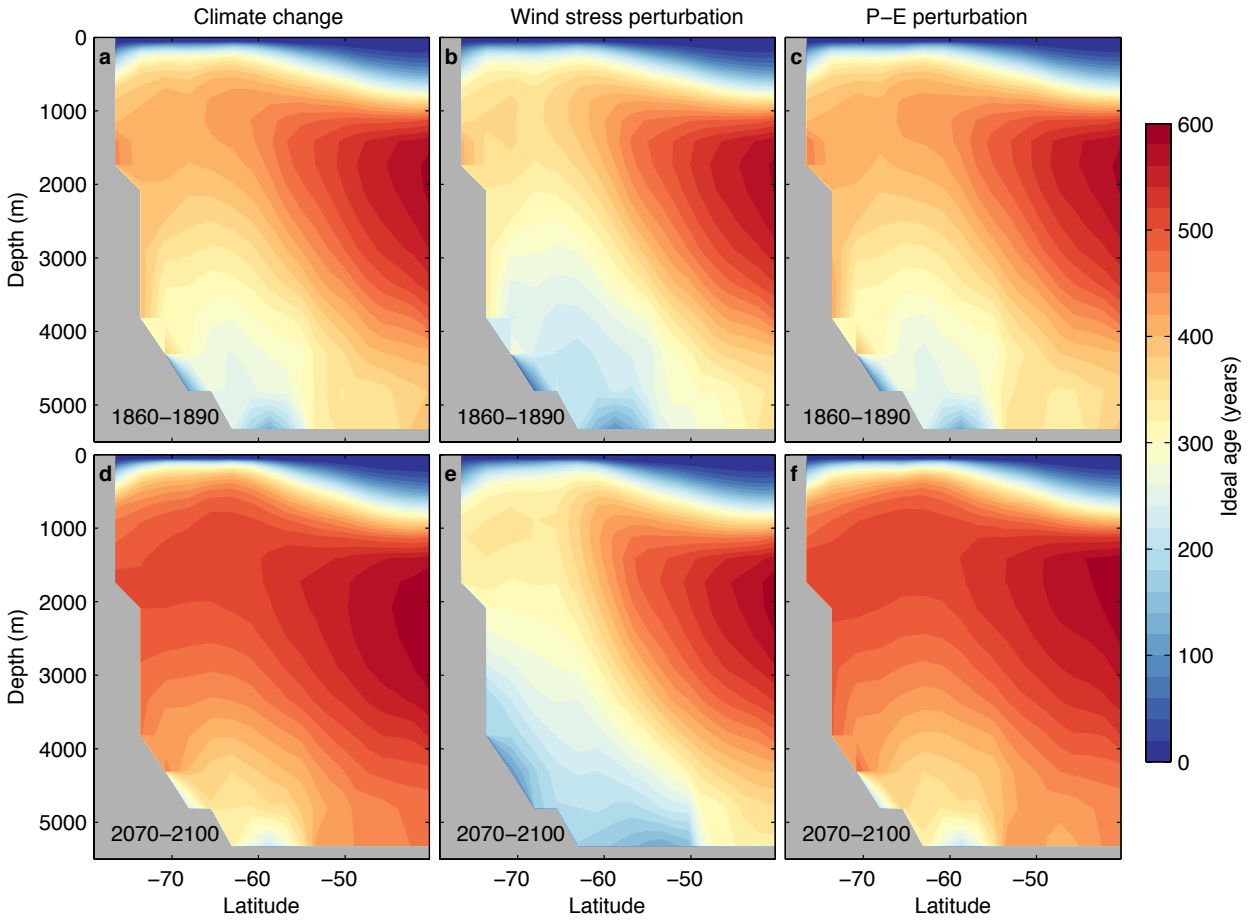

Figure S6: Zonal mean water age (since surface contact) in a depth versus latitude Southern Ocean profile for the CM2Mc model. Ensemble mean of three simulations shown for the 1860-1890 and 2070-2100 periods for the *Climate Change* (**a** and **d**, respectively), *Wind stress perturbation* (**b** and **e**) and *P-E perturbation* (**c** and **f**) experiments. The decrease in ventilation of intermediate and deep waters over 1860-2100 in the climate change experiments is not due to changes in wind stress, and hence must be explained by altered buoyancy fluxes. Changes in precipitation and evaporation south of 40°S alone cause a similar ventilation slowdown as that simulated under the full climate change forcing.

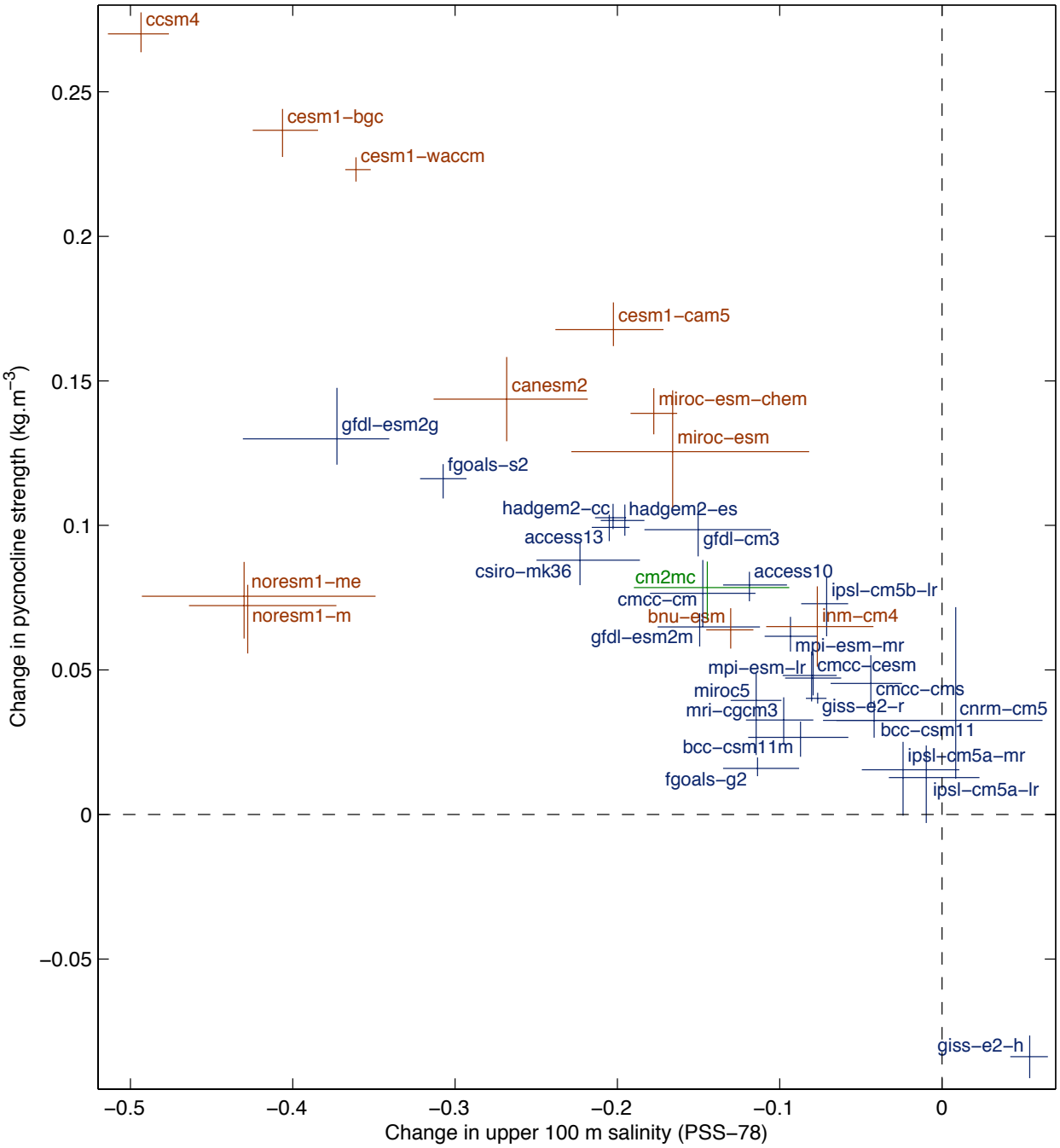

Figure S7: RCP8.5 changes and internal variability in southern polar ocean surface salinity and stratification in the CMIP5 model suite. Variables are annual averages over the region where the surface dynamic height relative to 1500 m is less than its minimum within Drake Passage, thus excluding both Antarctic Circumpolar Current and shelf waters. RCP8.5 changes (position of

crosses) refer to years 2050-2100 minus 1860-2005, and were corrected for drift by subtracting the linear pre-industrial control trends from the climate change time series. The range of unforced multidecadal variability is indicated by the vertical and horizontal bars, whose length is proportional to the maximum anomalies of all 50-year periods from the detrended pre-industrial control mean. Thus, RCP8.5 changes cannot be distinguished from unforced variability whenever these bars cross the origin, which is the case for the CNRM-CM5, IPSL-CM5A-LR and IPSL-CM5A-MR models only. Both convecting (blue) and non-convecting (brown) models are shown. The CM2Mc model ensemble is shown in green.

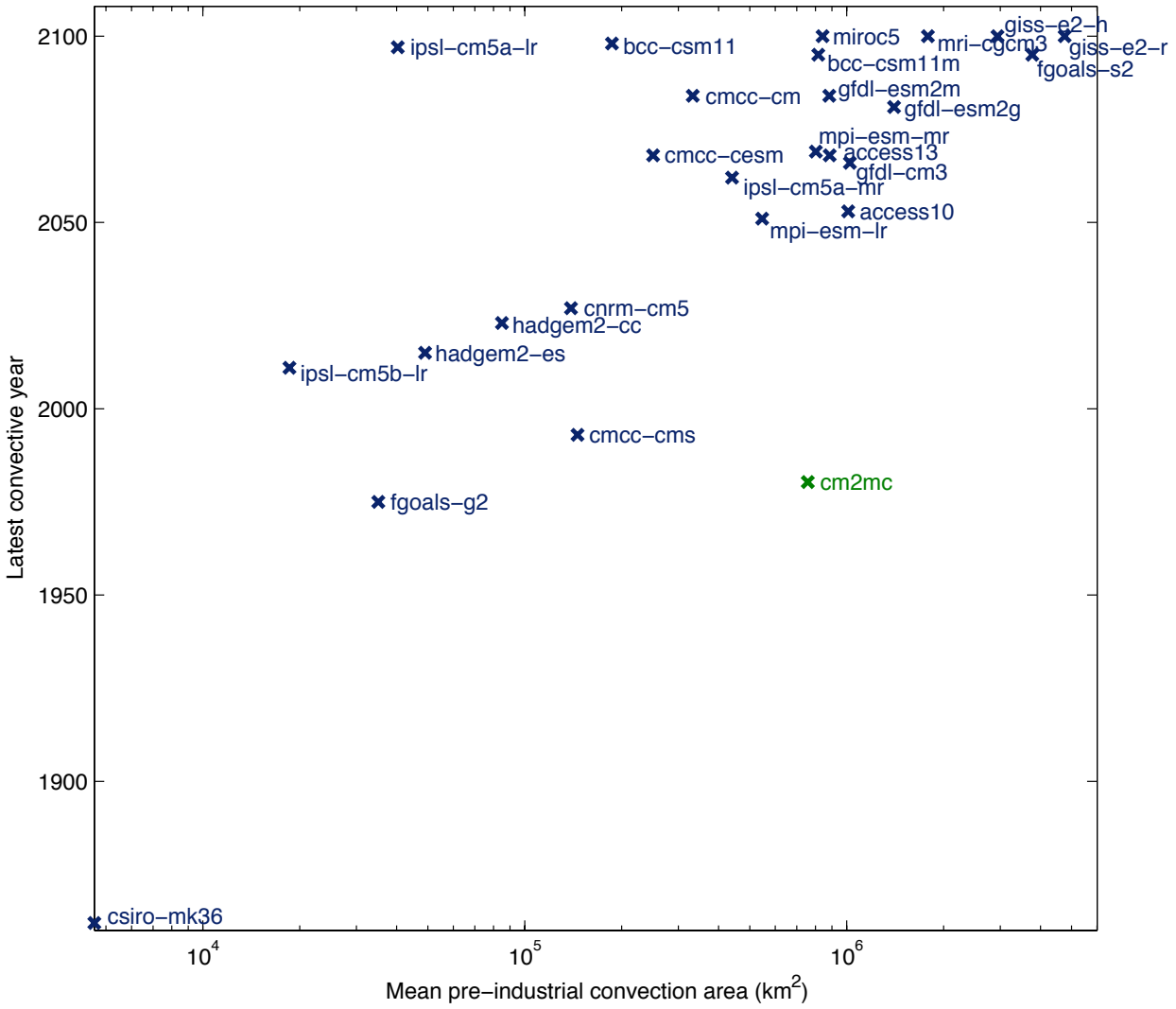

Figure S8: Latest convective year versus mean pre-industrial convection area in the 25 convecting CMIP5 models. Mean pre-industrial area is presented in log scale. The latest convective year corresponds to the last year of the climate change simulation (1860-2100) characterized by a convection area in excess of 100,000 km^2. Note that models with large convection areas tend to convect further in the 21st century. The three-member CM2Mc ensemble is shown in green.

Supplementary references:

31 Dunne, J. P. *et al*. GFDL's ESM2 global coupled climate-carbon Earth System Models. Part I: Physical formulation and baseline simulation characteristics. *J. Clim.* **25**, 6646-6665 (2012).

32 Martin, T., Adcroft, A. Parameterizing the fresh-water flux from land ice to ocean with interactive icebergs in a coupled climate model. *Ocean Model.* **34**, 111-124 (2010).

33 Large, W. G., McWilliams, J. C., Doney, S. C. Oceanic vertical mixing: a review and a model with a nonlocal boundary layer parameterization. *Rev. Geophys.* **32**, 363-403 (1994).

34 Bernardello, R. *et al*. Response of the ocean natural carbon storage to projected 21st century climate change. *J. Clim.* doi:10.1175/JCLI-D-13-00343.1, in press.

35 Meinshausen, M. *et al.* The RCP greenhouse gas concentrations and their extensions from 1765 to 2300. *Climatic Change* **109**, 213-241 (2011).

36 Delworth, T. L., Zeng, F. Simulated impact of altered Southern Hemisphere winds on the Atlantic meridional overturning circulation. *Geophys. Res. Lett.* **35**, L20708 (2008).

37 Yin, J. H. A consistent poleward shift of the storm tracks in simulations of 21st century climate. *Geophys. Res. Lett.* **32**, L18701 (2005).

38 Klinger, B. A., Marshall, J., Send, U. Representation of convective plumes by vertical adjustment. *J. Geophys. Res.* **101**, 18175-18182 (1996).

39 Rahmstorf, S. A fast and complete convection scheme for ocean models. *Ocean Model.* **101**, 9-11 (1993).

40 Hellmer, H. H. Impact of Antarctic ice shelf basal melting on sea ice and deep ocean properties. *Geophys. Res. Lett.* **31**, L10307 (2004).

41 Hellmer, H. H., Kauker, F., Timmermann, R., Determann, J., Rae, J. Twenty-first century warming of a large Antarctic ice-shelf cavity by a redirected coastal current. *Nature* **485**, 225-228 (2012).

42 Silva, T. A. M., Bigg, G. R., Nicholls, K. W. Contribution of giant icebergs to the Southern Ocean freshwater flux. *J. Geophys. Res.* **111**, C03004 (2006).

43 Bintanja, R., van Oldenborgh, G. J., Drijfhout, S. S., Wouters, B., Katsman, C. A. Important role for ocean warming and increased ice-shelf melt in Antarctic sea-ice expansion. *Nature Geosci.* **6,** 376-379 (2013).

44 Helm, K. P., Bindoff, N. L., Church, J. A. Changes in the global hydrological cycle inferred from ocean salinity. *Geophys. Res. Lett.* **37,** L18701 (2010).

45 Sen Gupta, A., Jourdain, N. C., Brown, J. N., Monselesan, D. Climate drift in CMIP5 models. *J. Clim.* **26**, 8597-8615 (2013).

46 Gaspar, P., Grégoris, Y., Lefevre, J-M. A Simple eddy kinetic energy model for simulations of the oceanic vertical mixing: tests at station Papa and Long-Term Upper Ocean Study site. *J. Geophys. Res.* **95**, 16179-16193 (1990).

47 Blanke, B., Delescluse, P. Variability of the tropical Atlantic Ocean simulated by a general circulation model with two different mixed-layer physics. *J. Phys. Oceanogr.* **23**, 1363-1388 (1993).

48 Kraus, E. B., Turner, J. S. A one-dimensional model of the seasonal thermocline II. The general theory and its consequences. *Tellus* **19**, 98-106 (1967).

49 Canuto, V. M., Howard, A., Cheng, Y., Dubovikov, M. S. Ocean turbulence. Part I: One-point closure model – momentum and heat vertical diffusivities. *J. Phys. Oceanogr.* **31**, 1413-1426 (2001).

50 Canuto, V. M., Howard, A., Cheng, Y., Dubovikov, M. S. Ocean turbulence. Part II: Vertical diffusivities of momentum, heat, salt, mass and passive scalars. *J. Phys. Oceanogr.* **32**, 240-264 (2002).

51 Thompson, L., Kelly, K. A., Darr, D., Hallberg, R. Buoyancy and mixed layer effects on the sea surface height response in an isopycnal model of the North Pacific. *J. Phys. Oceanogr.* **32**, 3657-3670 (2003).

52 Hallberg, R. In *Near-Boundary Processes and Their Parameterization: Proc. 'Aha Huliko'a Hawaiian Winter Workshop.* (Honolulu, HI, University of Hawaii at Manoa, 2003), pp. 187-203.

53 Mellor, G. L., Yamada, T. Development of a turbulence closure model for geophysical fluid problems. *Rev. Geophys.* **20**, 851-875 (1982).

54 Noh, Y., Kim, H. J. Simulations of temperature and turbulence structure of the oceanic boundary layer with the improved near-surface process. *J. Geophys. Res.* **104**, 15621-15634 (1999).

55 Noh, Y., Kang, Y. J., Matsuura, T., Iizuka, S. Effect of the Prandtl number in the parameterization of vertical mixing in an OGCM of the tropical Pacific. *Geophys. Res. Lett.* **32**, L23609 (2005).

56 Pacanowski, R. C., Philander, S. G. H. Parameterization of vertical mixing in numerical models of tropical oceans. *J. Phys. Oceanogr.* **11**, 1443-1451 (1981).

57 Oberhuber, J. M. Simulation of the Atlantic circulation with a coupled sea ice-mixed layer-isopycnal general circulation model. Part I: Model description. *J. Phys. Oceanogr.* **23**, 808-829 (1993).

58 Fetterer, F., Knowles, K., Meier, W., Savoie, M. Sea Ice Index. February 1979-2005. Boulder, Colorado USA: National Snow and Ice Data Center. (2002, updated 2009).